Li, L., et al., 2023, In situ Raman observations reveal that the gas fluxes of diffuse flow in hydrothermal systems are greatly underestimated: Geology, https://doi.org/10.1130/G50623.1

Supplementary Materials

In situ Raman observations reveal that the gas fluxes of diffuse flow in hydrothermal systems are greatly underestimated.

Lianfu Li[1,2,3], Zhendong Luan[1,2,3], Zengfeng Du[1,2], Shichuan Xi[1,2], Jun Yan[1,2], Xin Zhang[1,2,3*]

a. CAS Key Laboratory of Marine Geology and Environment & Center of Deep Sea Research, Institute of Oceanology, Center for Ocean Mega-Science, Chinese Academy of Sciences, Qingdao 266071, China.

b. Laboratory for Marine Geology, Pilot National Laboratory for Marine Science and Technology (Qingdao), Qingdao 266061, China.

c. University of Chinese Academy of Sciences, Beijing 100049, China.

Materials and Methods

The deployment of the Raman insertion probe system. The *in situ* Raman spectra of hydrothermal fluids were obtained using the Raman insertion probe system carried by the ROV *Faxian* (Fig. 1). The Raman insertion probe system contained a custom-designed N-RXNE-532-RA-SP spectrometer and a frequency-doubled Nd:YAG laser (532 nm) with an output power of 150 mW, both of which were manufactured by Kaiser Optical Systems, Inc. (USA). An Andor Technology (UK) DU-440A-BV-136 charge-coupled device (CCD) camera with 2048×512 pixels and a 27.6×6.9 mm image area was installed in the Raman insertion probe system. The spectrum (100-4325 cm^{-1}) was split into two lines (100-2100 and 2100-4325 cm^{-1}) on the surface of the CCD. Therefore, the spectral resolution of the Raman insertion probe system was approximately 1 cm^{-1} (Zhang et al., 2017). Before each deployment, the wavenumber and intensity calibration were processed with neon and

halogen lamps. HoloGRAMS software (Kaiser Optical Systems, Inc., Ann Arbor, USA) was used to acquire the Raman spectra of the hydrothermal fluids on deck, and each spectrum was acquired 8 times with a 4 s exposure time. All the acquired Raman spectra were processed with GRAM/AI software (Thermo Fisher Scientific, Inc., Waltham, USA) to subtract the baseline and determine the peak areas (peak height) of H_2O, CO_2, CH_4, H_2S and SO_4^{2-}.

Quantitative calibration of *in situ* Raman spectra. To establish quantitative calibration models of volatiles for high-temperature hydrothermal fluids, the relationship between the CH_4, CO_2, H_2S and SO_4^{2-} contents and their Raman signals were investigated at specified temperatures (Fig. S11). Analyte concentrations can be reflected by the intensity of the Raman spectrum based on the following formula:

$$R = IKP\sigma C \quad (1)$$

where R is the Raman signal intensity, I is the laser intensity, K represents the parameters of the instrument and samples, P is the optic path length, σ represents the Raman scattering cross section, and C is the concentration of the analyte (Lu et al., 2007, 2008). However, it is difficult to calibrate the concentration of the analyte based on the absolute Raman signal intensity because determining the values of I, K, and P is difficult, and the value of σ can be affected by molecular interactions. According to Placzek's ratio (Wopenka and Pasteris, 1986; Chou et al., 1990; Dubessy et al., 1989, 2001), the relative concentrations of two Raman-active species a and b in a solution phase, C_a and C_b (e.g., mole or mol%), are proportional to their Raman peak areas, A_a and A_b, respectively, by the following formula:

$$A_a/A_b = (C_a/C_b)(\sigma_a/\sigma_b)(\eta_a/\eta_b) = (C_a/C_b)(F_a/F_b) \quad (2)$$

where η and F are the instrumental efficiency and Raman quantification factor for peak area, respectively (Chou and Wang, 2017). H_2O is an ideal internal standard substance for quantifying the solute, and the concentrations of dissolved CH_4, H_2S and SO_4^{2-} (in molality) can be determined using the peak area ratios of $A(CH_4)/A(H_2O)$, $A(H_2S)/A(H_2O)$, *and* $A(SO_4^{2-})/A(H_2O)$. The peak areas of CH_4, H_2S and SO_4^{2-} were determined within spectral ranges of 2870-2940 cm^{-1}, 2530-2650 cm^{-1} and 960-1000 cm^{-1}, respectively (Zhang et al., 2011; Li et al., 2018, 2020). For the calibration of CO_2, the peak height $H(CO_2)$ rather than the peak area $A(CO_2)$ of CO_2 was used in Eq. (2) (Fig. S11), because the hot bands are very pronounced at high temperatures (> 200°C), which disturbs the determination of the peak area of the symmetric stretching mode of CO_2 (Rosso and Bodnar, 1995). The peak height of CO_2 was determined by the relative height from the highest peak to the baseline at 1344-1420 cm^{-1}. The OH bending band of H_2O was selected as the reference peak and its peak area and height were determined within a spectral range of 1450-1830 cm^{-1} (Li et al., 2018).

Hydrothermal fluid environments were simulated using a custom-designed deep-ocean extreme environment simulation system that mainly consists of a high-temperature and high-pressure reactor, a pressurization system and a temperature control system (Fig. S12) (Li et al., 2020). An immersion probe used to acquire Raman spectra was inserted into the reactor to ensure that the probe could directly contact the fluid samples. In this study, the temperatures and pressures of the deep-ocean extreme environment simulation system were maintained in the ranges of 2 to 300°C and 0.1 to 40 MPa, respectively. Raman spectra of dissolved CH_4, CO_2, H_2S and SO_4^{2-} with various concentrations were collected, and the peak areas or peak heights for CH_4, CO_2, H_2S, SO_4^{2-} and H_2O were determined

using GRAM/AI software. The quantitative calibration models of CH_4, CO_2, H_2S and SO_4^{2-} established based on the relationship between the concentration and the peak area (height) ratio are displayed in Fig. S11 (Li et al., 2018, 2020; Zhang et al., 2011).

Calibration of CO_2, CH_4, H_2S and SO_4^{2-} endmember concentrations. The volatile concentrations directly calculated based on the quantitative calibration models cannot represent the real values of hydrothermal fluid for seawater entrainment during *in situ* measurements. As a stable and conserved element in seawater, Mg has been widely used for the endmember concentration calibration of hydrothermal fluid components (Seewald et al., 2002; Von Damm et al., 1985). However, Raman spectroscopy cannot be used for the detection of Mg concentrations in seawater and hydrothermal fluids. In this study, SO_4^{2-} was taken as an indicator for assessing the seawater entrainment extent. Considering that the endmember concentrations of SO_4^{2-} may be influenced by the precipitation and redissolution of anhydrite, we first determined the endmember value of sulfate based on the relationship between Mg and SO_4^{2-} concentrations of the gas-tight samples (Fig. S6). The SO_4^{2-} values of Site 1, 6 and 14 vents decrease linearly to ~ 0 mmol/kg with Mg extrapolated to zero, indicating that the endmember hydrothermal fluids in the Iheya North field are free from SO_4^{2-}. Three Raman spectra of ambient seawater at the North Big Chimney mound collected with the Raman insertion probe system were used to calculate the SO_4^{2-} endmember value of seawater, and the average SO_4^{2-} concentration was determined to be 28.6 mmol/kg. Finally, the CO_2, CH_4, H_2S and SO_4^{2-} endmember concentrations can be calculated using SO_4^{2-}-Volatiles diagrams (Fig. S7).

Fluid temperature measurements. The temperatures of hydrothermal fluids in the North Big Chimney mound were measured via a K-type Omega thermocouple (TJ100-CA316SS-

316U-20-SMPW-M) with an upper range limit of 650°C and a precision of 0.75%. To ensure the reliability of the temperature measurements, the measuring position of the thermocouple sensor was held as stationary as possible. To minimize the effect of seawater entrainment on fluid temperature measurements, the temperature probe is inserted as deeply as possible into the orifice of the chimney. However, even so, it is still difficult to accurately measure the temperature of the diffuse flow fluid.

Hydrothermal fluid sampling. The hydrothermal fluids of the North Big Chimney mound were sampled using a custom-designed gas-tight sampler with a 150 ml sample volume capacity. Due to the limitation of underwater operation time and carrying capacity of ROV, the gas-tight fluid samples were collected only at Site 1, 6 and 14 vents. To minimize the loss of gases and the precipitation of minerals, the gas-tight samples were processed after the ROV returned to the ship (no more than 24 hours). The gas samples in the gas-tight bottles were transferred to gas sample bags to recover the gas components. The concentration of Mg in the fluid samples was measured by inductively coupled plasma atomic emission spectrophotometry (ICP–AES, Thermo Scientific Corp., Ltd) after appropriate sample dilution using Milli-Q deionized water. The chlorine and sulfate concentrations of the vent fluids were analyzed by ion chromatography (IC) (DIONEX ICS-5000) with a 5% error.

Heat output measurements. The heat fluxes (H) for the diffuse flow and focused flow were calculated as follows (Rona and Trivett, 1992; Ramondenc et al., 2006):

$$H = C_p v \Delta T A \tag{3}$$

where v is the flow velocity of hydrothermal fluid, ΔT is the temperature difference between the vent fluid and ambient seawater, $C_p = \rho_p c_p \approx 4 \times 10^6$ J/(m^3°C) is the

volumetric heat capacity of the fluid, with ρ_p and c_p being the fluid density and specific heat of the vent fluid, respectively, and A is the hydrothermal fluid releasing area.

Volatile flux ratio of diffuse flow to focused flow calculation.

We define *R* as the ratio of heat flux (*H*) to volatile flux (*V*), common parameters for calculating *H* and *V* can be offset:

$$R = \frac{H}{V} = \frac{\Delta T C_p}{C} \tag{4}$$

The ratio between *R* value of diffuse flow (R_d) and *R* value of focused flow (R_f) can be calculated by the following equation:

$$\frac{R_d}{R_f} = \frac{H_d/V_d}{H_f/V_f} = \frac{\Delta T_d/C_d}{\Delta T_f/C_f} \tag{5}$$

Then, the ratio of diffuse flow (V_d) and focused flow (V_f) in terms of volatile fluxes can be calculated:

$$\frac{V_d}{V_f} = \frac{\Delta T_f}{\Delta T_d}\frac{C_d}{C_f}\frac{H_d}{H_f} \tag{6}$$

where ΔT_d and ΔT_f represent the temperature difference between the diffuse and focused fluids and the ambient seawater, respectively, and C_d and C_f represent the measured concentration of gas volatiles in the diffuse and focused fluids, respectively.

Flow rate measurements

A custom-made underwater ruler was designed to measure the flow velocities. The flow velocities of the focused vent were measured by placing the customized ruler that was marked with 10 cm intervals vertically on the orifice of each vent, and those of the diffuse sites were measured by placing the customized ruler vertically on the seafloor. The flow velocities were measured by advancing the video image frame-by-frame and timing the

rise of eddies or particles in the initial 10 cm interval (Rona and Trivett, 1992; Ramondenc et al., 2006). For low velocity diffuse areas, the turbine flow meter also was used to determine flow rates of diffuse flow, and combined with the means of video analysis to determine the flow rate of low velocity hydrothermal fluid.

Estimation of the diffuse flow and focused flow areas

In this study we classify the discharge types of fluids in the North Big Chimney mound based on fluid flow rate, emission state, and vent/chimney morphology. The boundaries of the diffuse and focused flow sites were determined through video and image analysis, and the precise location information of the diffuse and focused flow site boundaries was determined by the ultrashort baseline positioning system of the ROV. The sizes of the specific areas of diffuse and focused flow sites were estimated based on the obtained boundary location information using Surfer software (Golden Software Inc., Colorado, USA). Given that not all the diffuse and focused flow zones have fluid discharge, the proportions of the fluid release area used to measure the flux of hydrothermal fluid were estimated to be 5%-20% and 1%-5% for diffuse and focused flow areas, respectively.

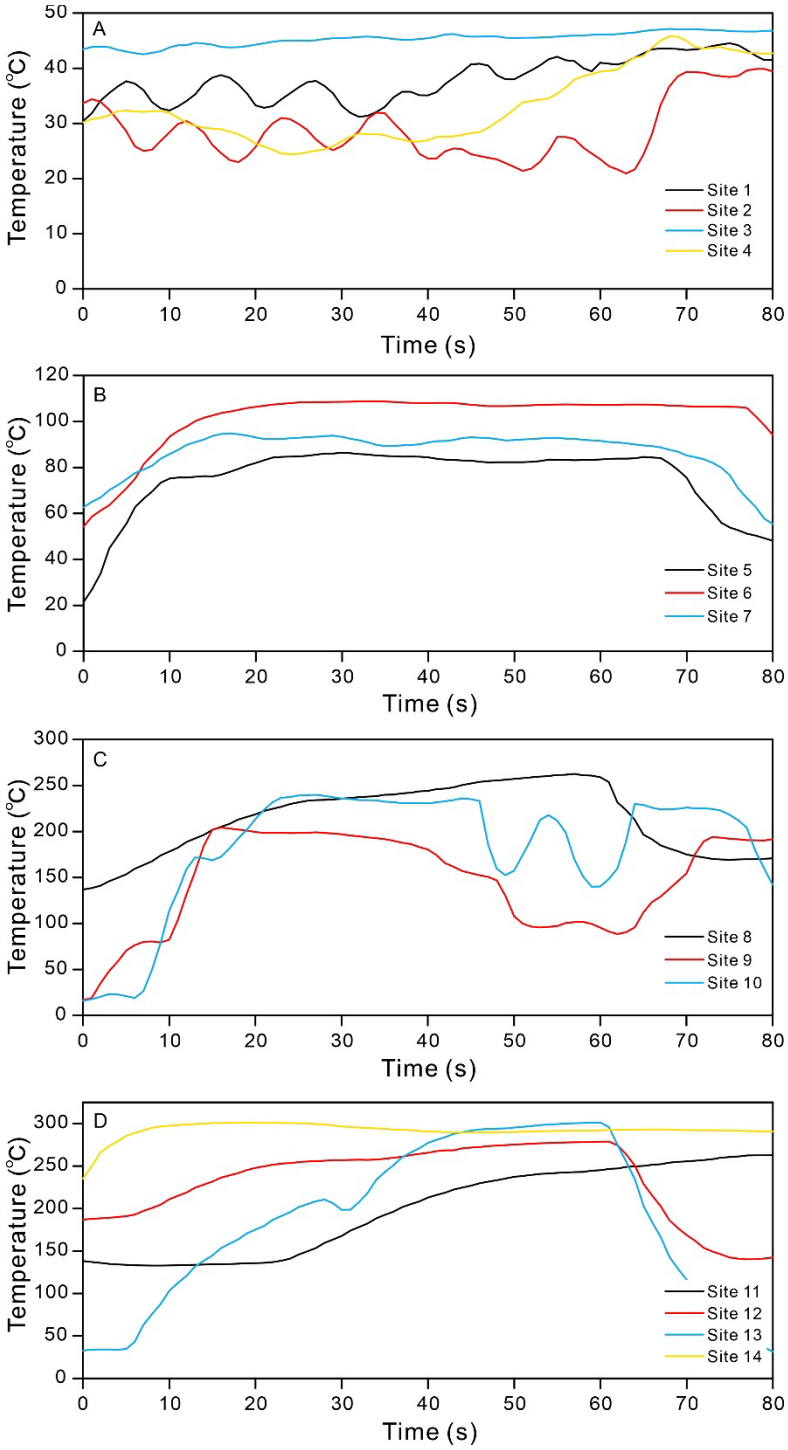

Fig. S1. Hydrothermal fluid temperatures at Site 1 to 14 vents in the North Big Chimney mound measured through a K-type Omega thermocouple. The temperature of the hydrothermal fluids is the relatively stable temperature taken during measurement. The temperatures of hydrothermal fluids for these 14 vents range from ~ 30 to 302°C.

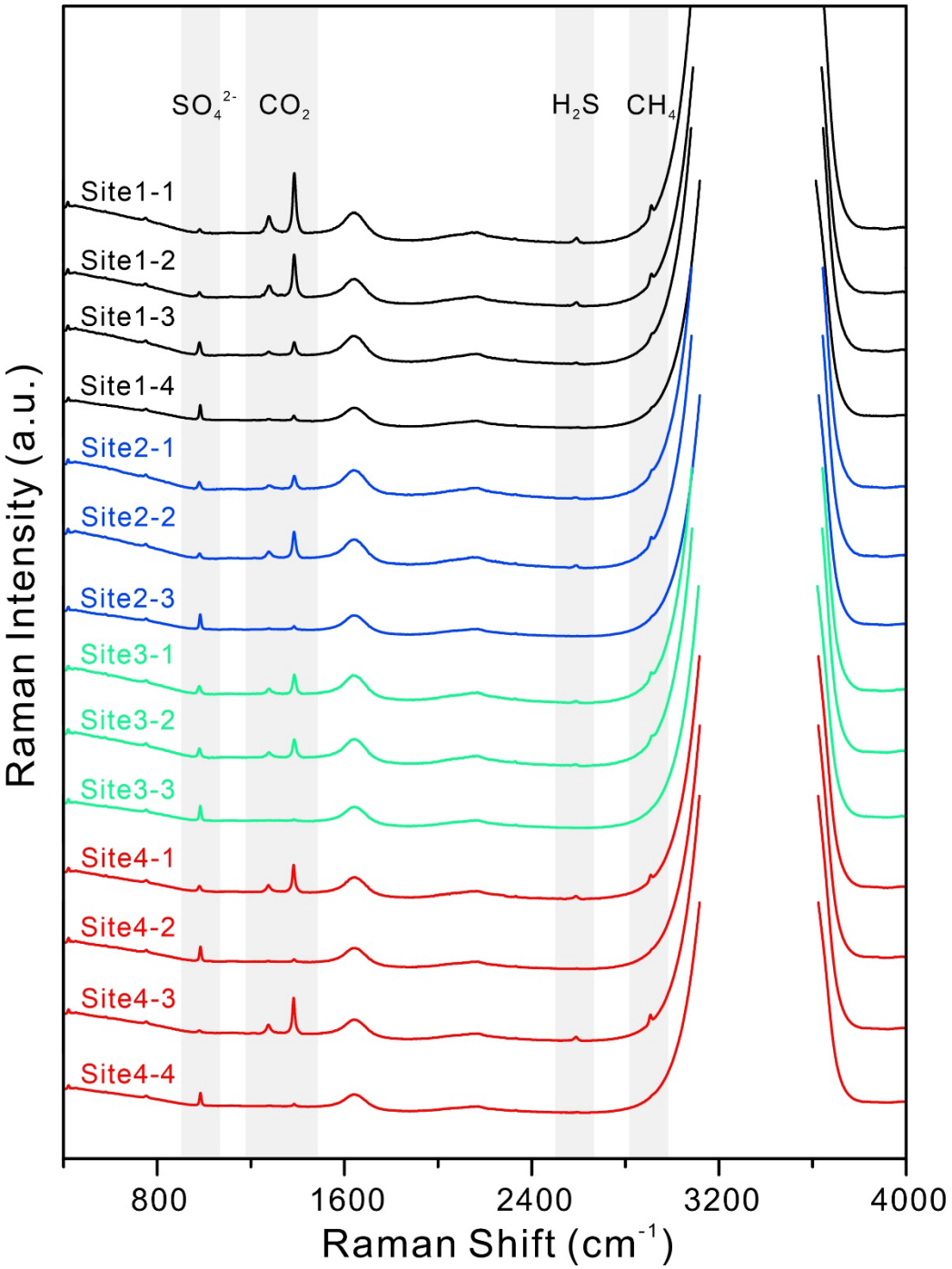

Fig. S2. *In situ* Raman spectra of hydrothermal fluids emitted from Site 1 to 4 vents. Raman spectra of Site 1 to 4 vents were collected within temperature ranges of approximately 30-45°C, 30-35°C, 40-47°C and 30-40°C, respectively. The endmember concentrations of CH_4, CO_2 and H_2S for the low-temperature diffuse flows (Site 1 to 4 vents) were derived from the Raman spectra obtained by the Raman insertion probe system. Concentrations of H_2S for Site 2-3, Site 3-3 and Site 4-2 and CH_4 for Site 3-3 were below the limit of detection of Raman insertion probe system.

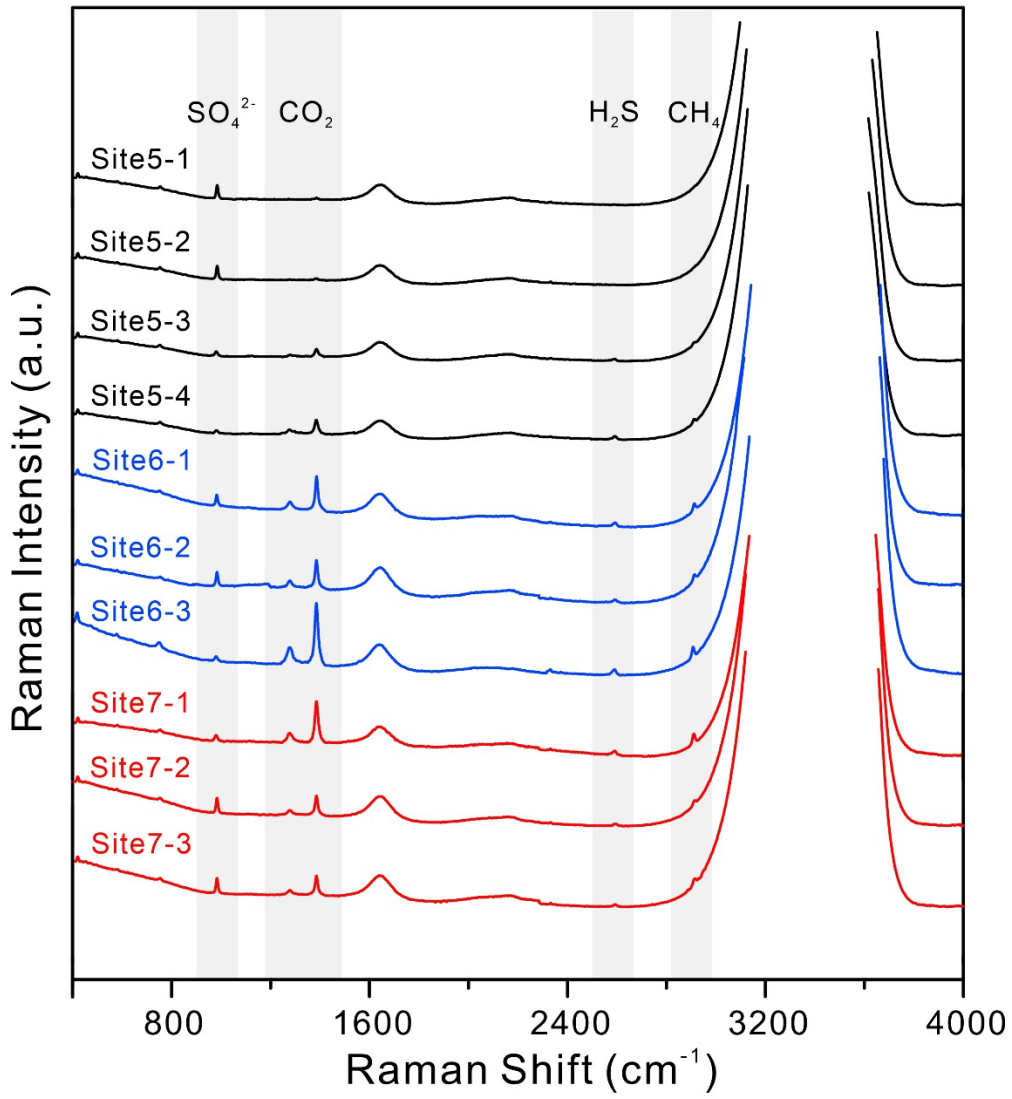

Fig. S3. *In situ* Raman spectra of hydrothermal fluids emitted from Site 5 to 7 vents. Raman spectra of Site 5 to 7 vents were collected within temperature ranges of approximately 77-88°C, 95-109°C and 87-95°C, respectively. The endmember concentrations of CH_4, CO_2 and H_2S for the middle-temperature diffuse flows (Site 5 to 7 vents) were derived from the Raman spectra obtained by the Raman insertion probe system. Concentrations of H_2S and CH_4 for Site 5-1 and Site 5-2 were below the limit of detection of Raman insertion probe system.

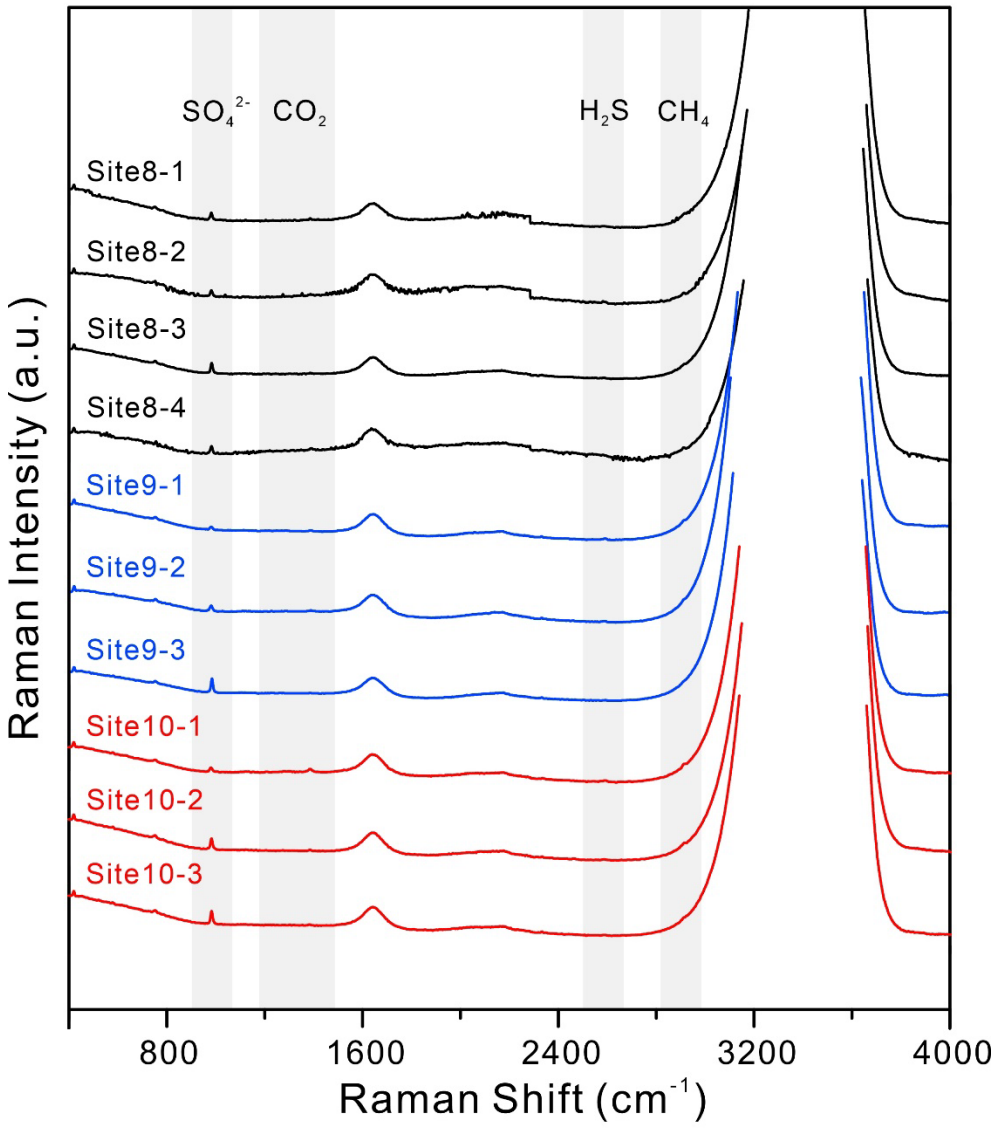

Fig. S4. *In situ* Raman spectra of hydrothermal fluids emitted from Site 8 to 10 vents. Raman spectra of Site 8 to 10 vents were collected within temperature ranges of approximately 225-260°C, 160-202°C, and 190-240°C, respectively. The endmember concentrations of CH_4, CO_2 and H_2S for the high-temperature diffuse flows (Site 8 to 10 vents) were derived from the Raman spectra obtained by the Raman insertion probe system. Concentrations of H_2S and CH_4 for Site 9-3 were below the limit of detection of Raman insertion probe system.

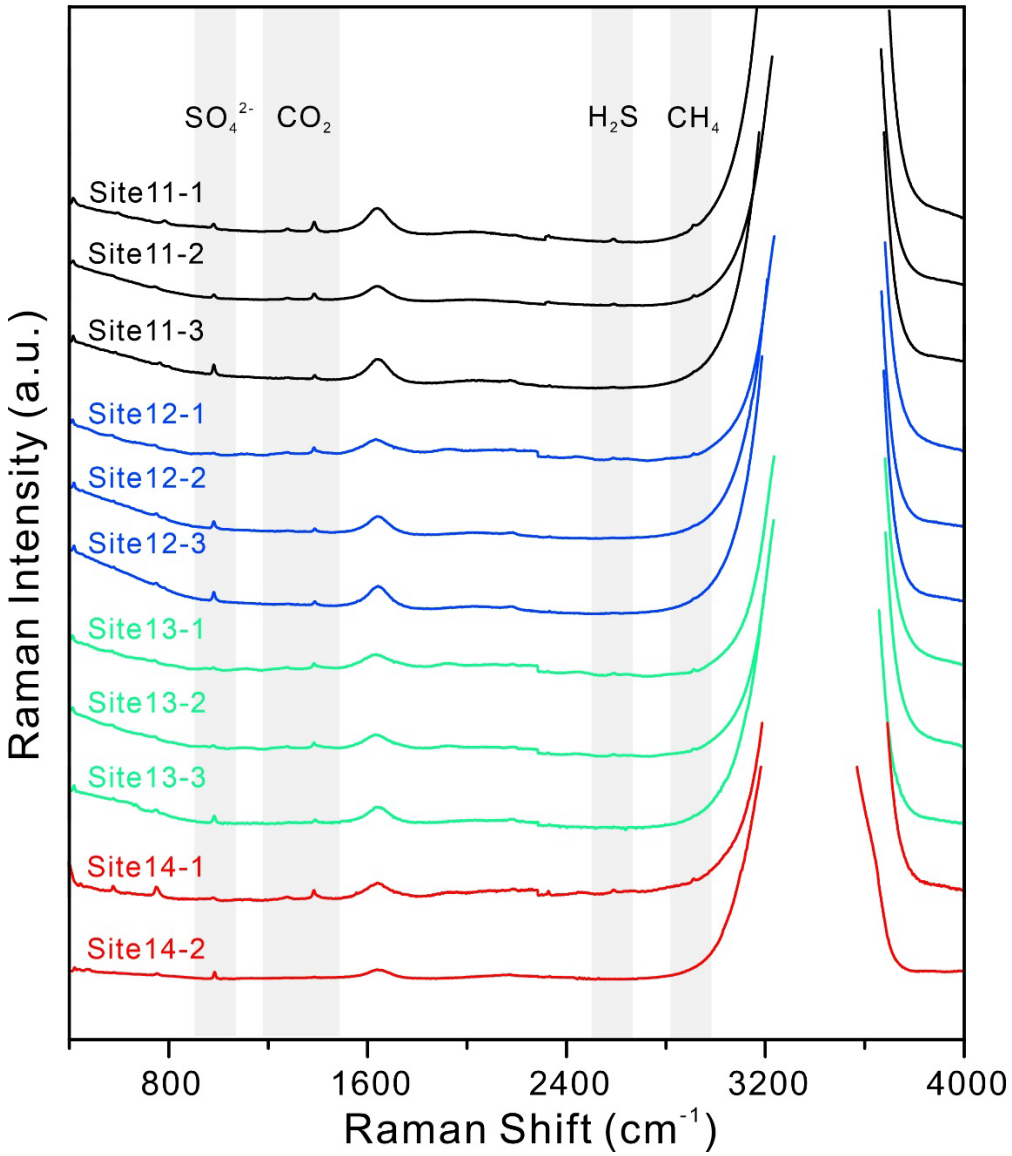

Fig. S5. *In situ* Raman spectra of hydrothermal fluids emitted from Site 11 to 14 vents. Raman spectra of Site 11 to 14 vents were collected within temperature ranges of approximately 240-266°C, 260-280°C, 280-300°C and 288-302°C, respectively. The endmember concentrations of CH_4, CO_2 and H_2S for the focused flows (Site 11 to 14 vents) were derived from the Raman spectra obtained by the Raman insertion probe system. Concentrations of H_2S and CH_4 for Site 14-2 were below the limit of detection of Raman insertion probe system.

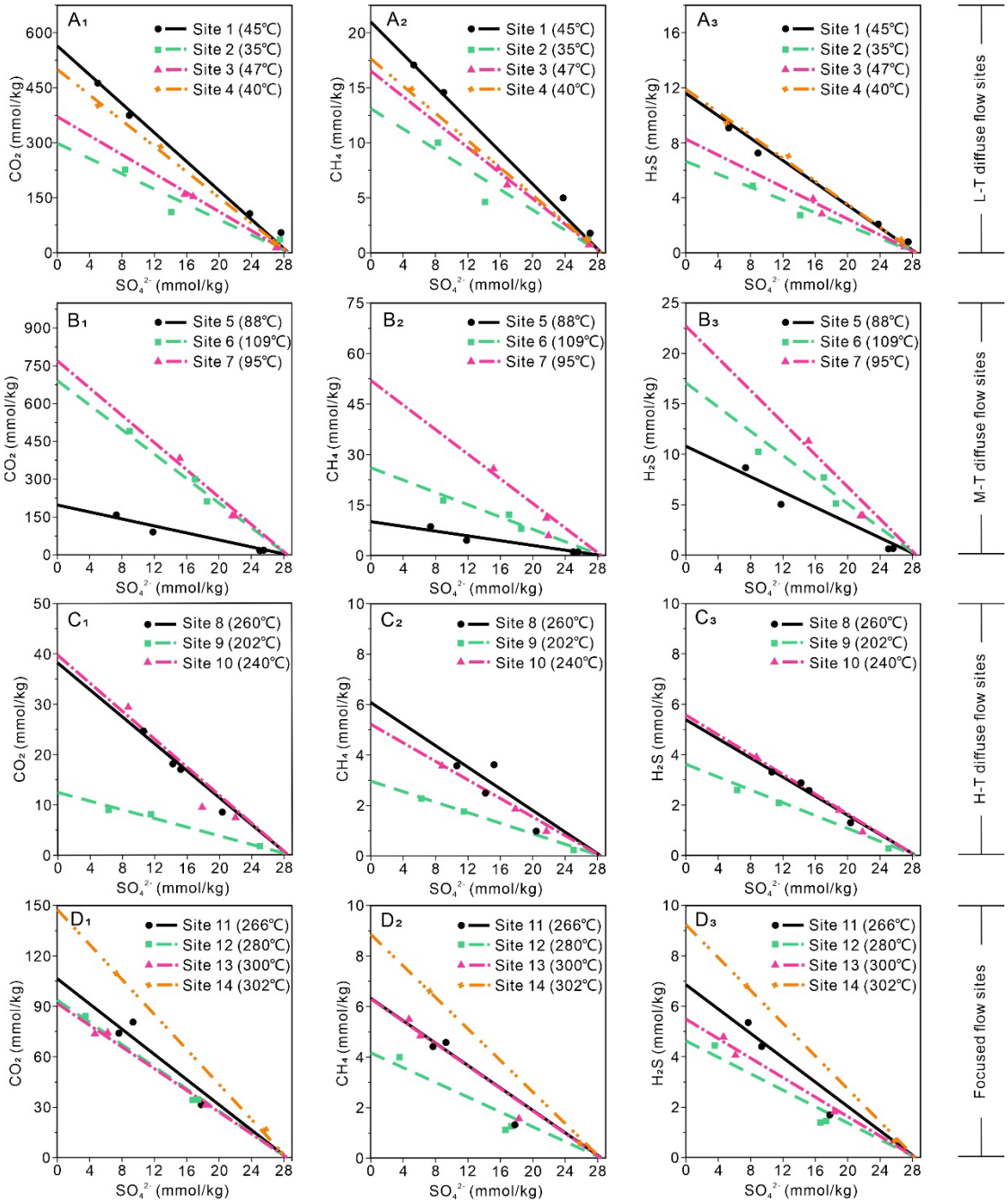

Fig. S6. Endmember concentrations of CO_2, CH_4, and H_2S for 14 sites at the North Big Chimney mound, Iheya North hydrothermal field calibrated based on SO_4^{2-}. Endmember concentrations of SO_4^{2-} for seawater and hydrothermal fluid were assumed to be 28.6 and 0 mmol/kg, respectively.

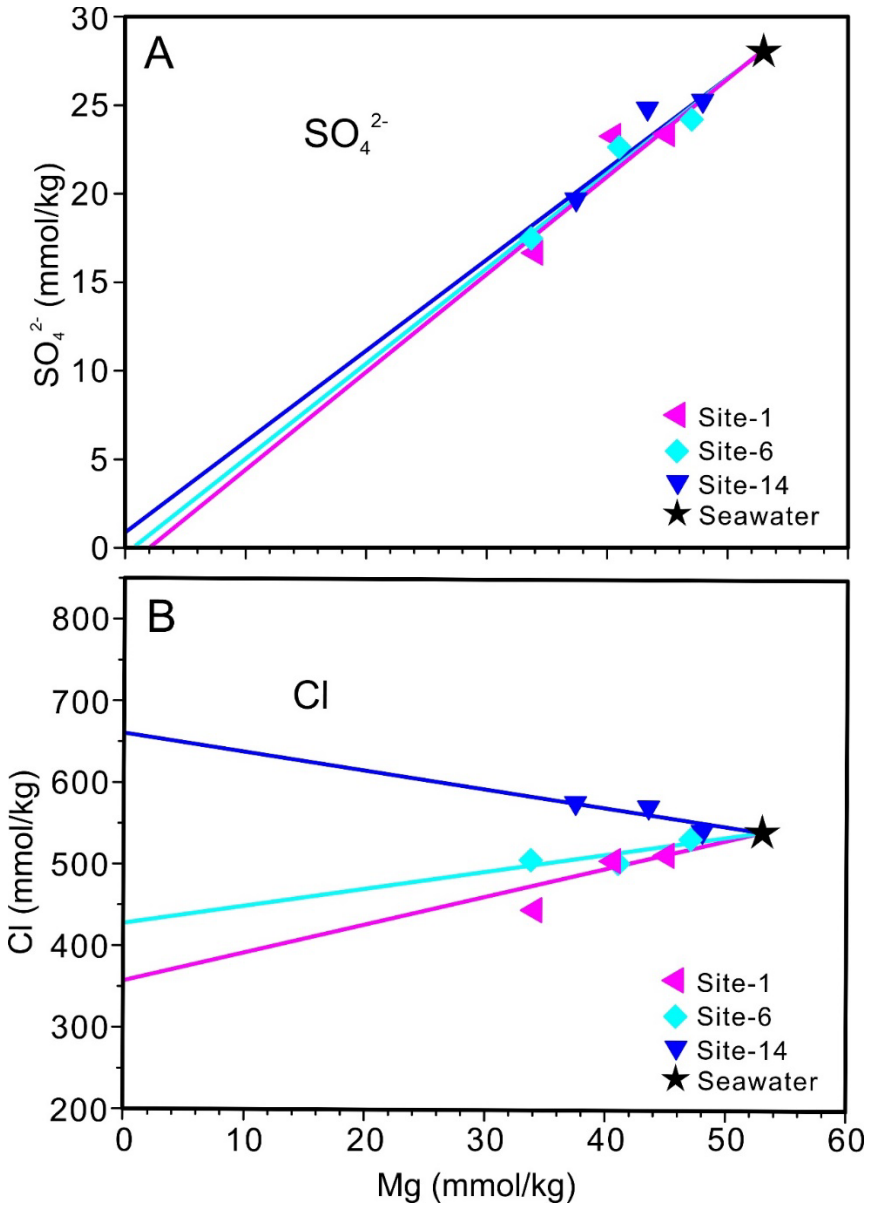

Fig. S7. Endmember concentrations of SO_4^{2-} and Cl^- for hydrothermal fluids of Site 1, 6 and 14 vents calculated based on Mg. Endmember concentrations of Mg for seawater and hydrothermal fluid were assumed to be 53 and 0 mmol/kg, respectively.

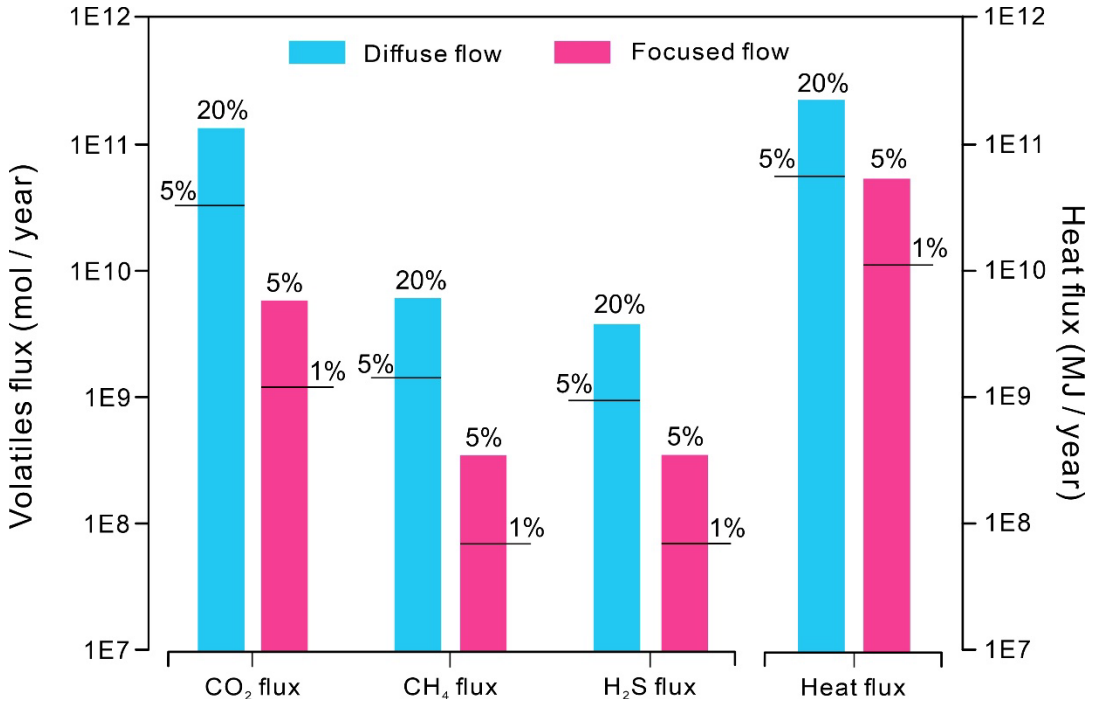

Fig. S8. Fluxes of volatiles and heat for diffuse flow and focused flow at the North Big Chimney mound. The proportion of the hydrothermal fluid release area is estimated to be 5% to 20% and 1% to 5% of the diffuse flow area and focused flow area, respectively. The specific values of heat flux and volatile flux are displayed in Table S3.

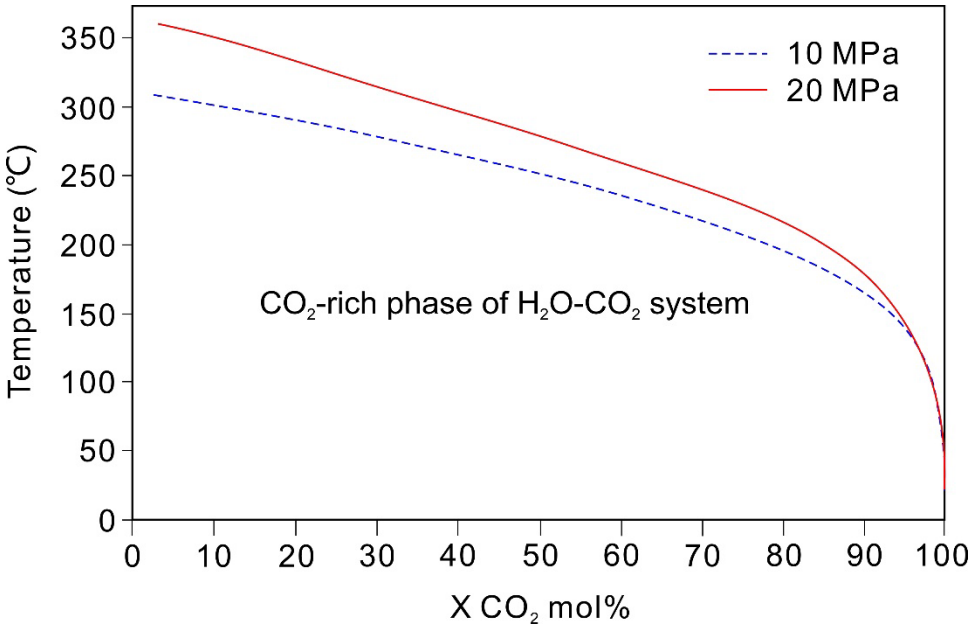

Fig. S9. Phase equilibrium in the H_2O-CO_2 system at various pressures and temperatures. There is a negative correlation between the phase equilibrium temperature and CO_2 fraction concentration under the same pressure conditions for the CO_2-rich phase of H_2O-CO_2 system. (Raw data from Fig. 3 of Dubacq et al., 2013)

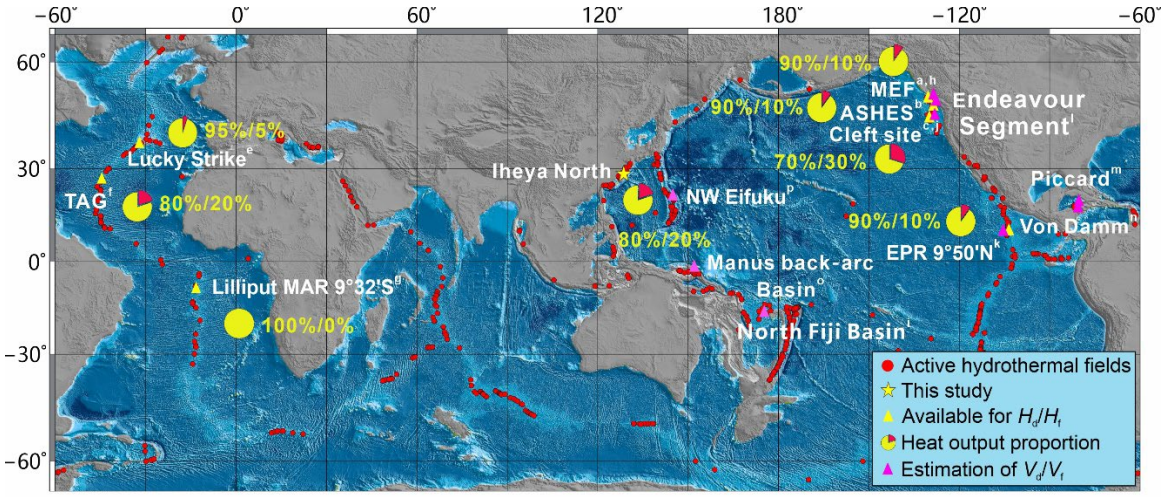

Available for H_d/H_t:

[a]Main Endeavour Field (MEF) (*13*)
[b]ASHES (*42*)
[c]Cleft site (*47*)
[d]East Pacific Rise (EPR) 9°50'N (*43, 46*)
[e]Lucky Strike (*49*)
[f]Trans-Atlantic Geotraverse (TAG) (*48*)
[g]Lilliput MAR 9°32'S (*50*)

Estimation of V_d/V_f:

[h]Main Endeavour Field (MEF) (*51*)
[i]NFB North Fiji Basin (*54*)
[j]Cleft site (*55*)
[k]East Pacific Rise (EPR) 9°50'N (*36*)
[l]Endeavour Segment (*52*)
[m]Piccard (*53*)
[n]Von Damm (*53*)
[o]Manus back-arc Basin (*56*)
[p]NW Eifuku (*57*)

Fig. S10. Estimation of the proportion of volatile flux released by diffuse flow and focused flow using the reported heat flux ratio. The red points and the yellow pentagrams represent active hydrothermal fields worldwide and the North Big Chimney mound in the Iheya North hydrothermal field, respectively. The red–yellow pie chart represents the heat output proportion for the diffuse and focused flows. The yellow triangle and pink triangle represent the hydrothermal sites with available heat output proportion and estimation of volatile flux proportion for the diffuse and focused flows, respectively.

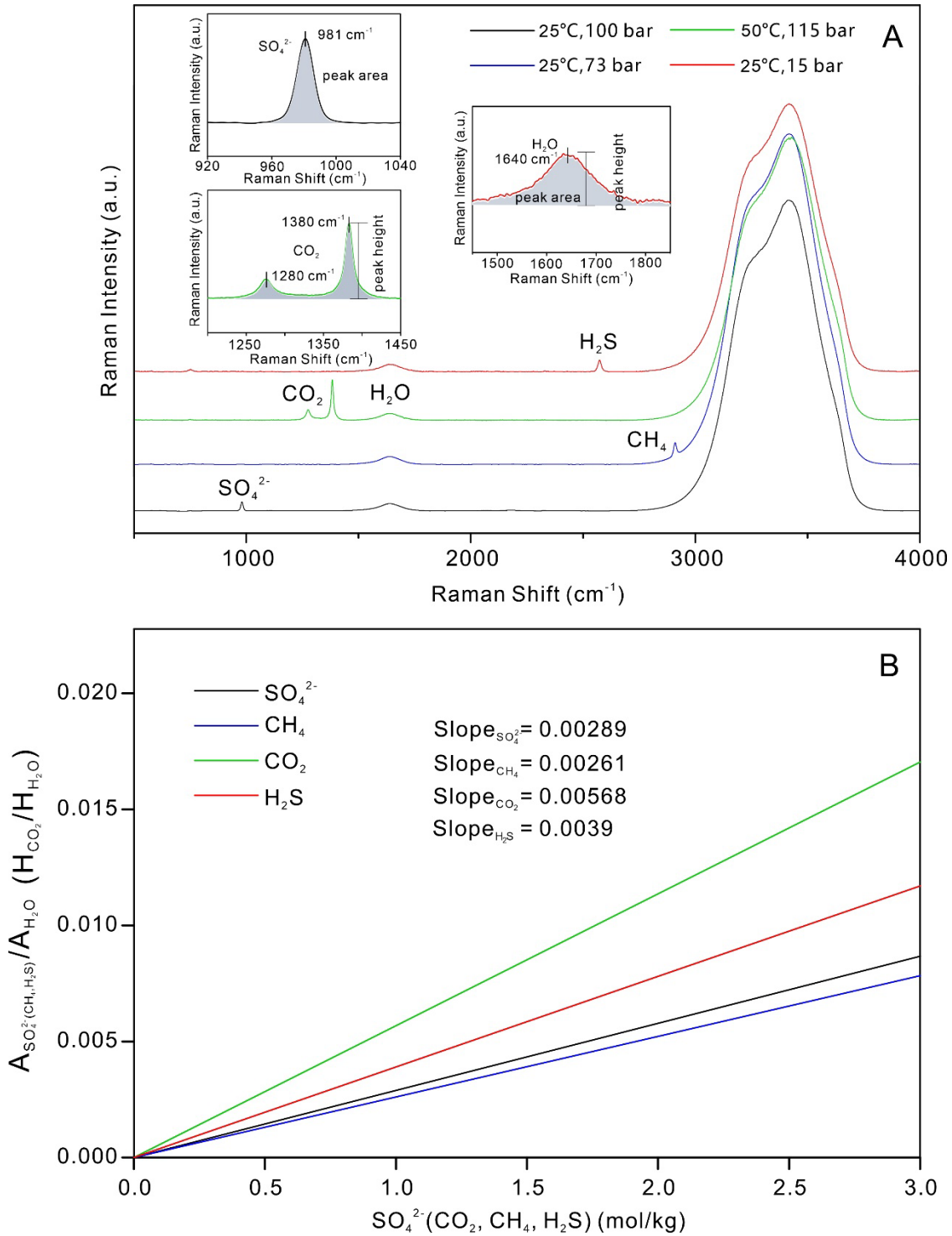

Fig. S11. Raman spectra and calibration models of dissolved CO_2, CH_4, H_2S and SO_4^{2-}. (A) Raman parameters of CO_2, CH_4, H_2S and SO_4^{2-} to develop the calibration models. (B) The quantitative models of volatile gases were established within the ranges of 2 to 300°C and 0.1 to 40 MPa, and the slopes for the calibration lines of CO_2, CH_4, H_2S and SO_4^{2-} were determined to be 0.00568, 0.00261, 0.0039 and 0.00289, respectively.

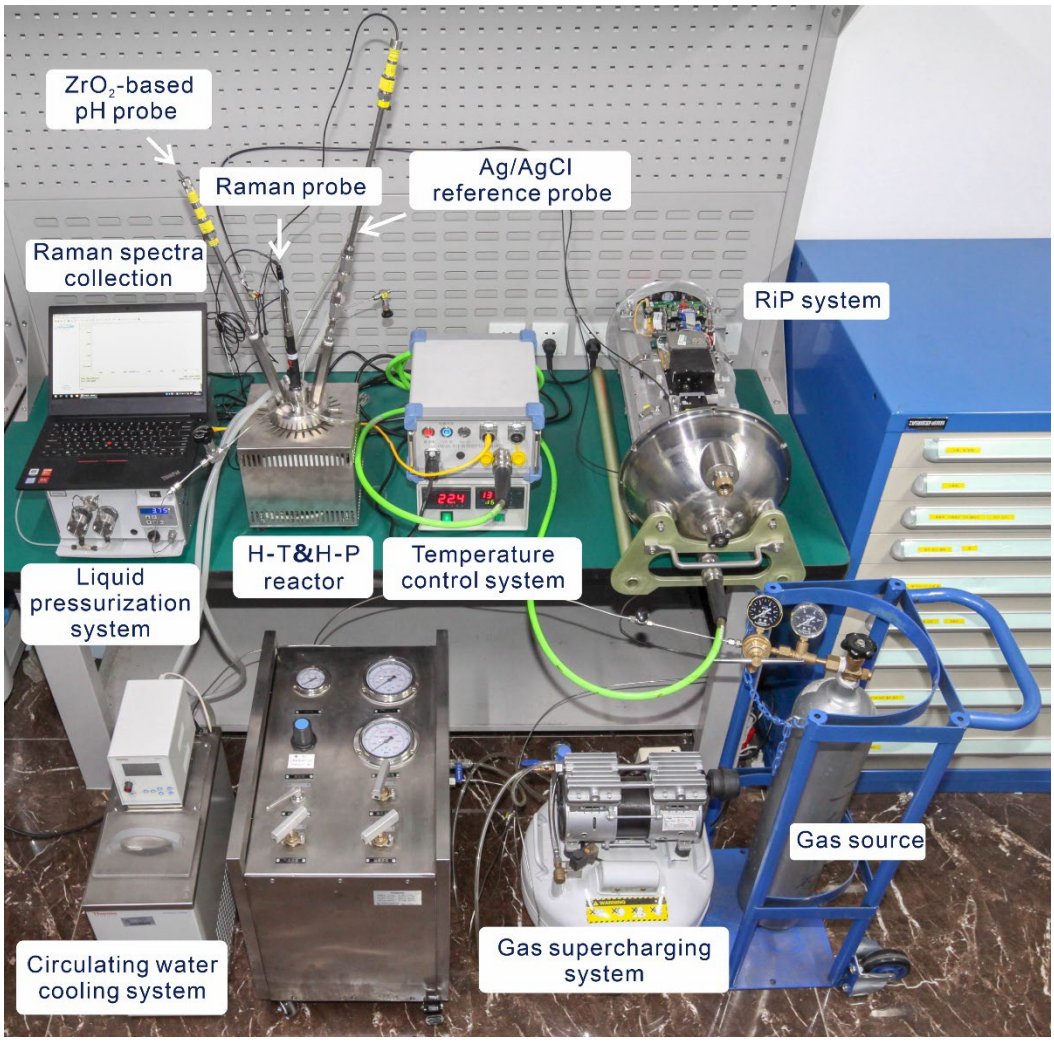

Fig. S12. Photograph of the deep-sea extreme environmental simulation system. The equipment used for the quantitative calibration experiments in the laboratory mainly includes the Raman insertion probe system, high temperature and high pressure reactor, gas supercharging system, liquid pressurization system and temperature control system, etc.

Table S1. The concentrations of SO_4^{2-}, CH_4, H_2S and CO_2 derived from *in situ* Raman spectroscopy measurements

	$PAR_{SO4/H2O}$[a]	$PAR_{CH4/H2O}$[b]	$PAR_{H2S/H2O}$[c]	$PHR_{CO2/H2O}$[d]	SO_4^{2-} (mmol/kg)[e]	CH_4 (mmol/kg)[f]	H_2S (mmol/kg)[g]	CO_2 (mmol/kg)[h]
Site-1-1	0.0154	0.0445	0.0359	2.6635	5.3	17.0	9.2	468.9
Site-1-2	0.0258	0.0374	0.0285	2.1378	8.9	14.3	7.3	376.4
Site-1-3	0.0687	0.0130	0.0082	0.6072	23.8	5.0	2.1	106.9
Site-1-4	0.0802	0.0046	0.0035	0.3407	27.8	1.8	0.9	60.0
Site-2-1	0.0406	0.0122	0.0104	0.6318	14.1	4.7	2.7	111.2
Site-2-2	0.0240	0.0261	0.0192	1.2957	8.3	10.0	4.9	228.1
Site-2-3	0.0794	0.0036	0.0011	0.2026	27.5	1.4	<LOD	35.7
Site-3-1	0.0455	0.0204	0.0155	0.9458	15.8	7.8	4.0	166.5
Site-3-2	0.0483	0.0161	0.0108	0.8934	16.7	6.2	2.8	157.3
Site-3-3	0.0781	0.0000	0.0000	0.0875	27.0	<LOD	<LOD	15.4
Site-4-1	0.0366	0.0238	0.0272	1.6410	12.7	9.1	7.0	288.9
Site-4-2	0.0776	0.0026	0.0027	0.1523	26.8	1.0	<LOD	26.8
Site-4-3	0.0144	0.0388	0.0367	2.2811	5.0	14.9	9.4	401.6
Site-4-4	0.0770	0.0033	0.0032	0.1791	26.6	1.3	0.8	31.5
Site-5-1	0.0739	0.0000	0.0032	0.1042	25.6	<LOD	<LOD	18.4
Site-5-2	0.0722	0.0000	0.0000	0.1104	25.0	<LOD	<LOD	19.4
Site-5-3	0.0344	0.0127	0.0201	0.4925	11.9	4.9	5.1	86.7
Site-5-4	0.0210	0.0213	0.0339	0.9251	7.3	8.2	8.7	162.9
Site-6-1	0.0493	0.0316	0.0311	1.7159	17.0	12.1	8.0	302.1
Site-6-2	0.0535	0.0218	0.0210	1.2011	18.5	8.3	5.4	211.5
Site-6-3	0.0259	0.0442	0.0424	2.7852	8.9	16.9	10.9	490.3
Site-7-1	0.0440	0.0667	0.0449	2.1677	15.2	25.6	11.5	381.6
Site-7-2	0.0631	0.0166	0.0157	0.9306	21.8	6.4	4.0	163.8
Site-7-3	0.0627	0.0303	0.0157	0.9205	21.7	11.6	4.0	162.1
Site-8-1	0.0307	0.0093	0.0130	0.1416	10.6	3.6	3.3	24.9
Site-8-2	0.0410	0.0066	0.0110	0.1023	14.2	2.5	2.8	18.0

Site-8-3	0.0439	0.0095	0.0096	0.0972	15.2	3.6	2.5	17.1
Site-8-4	0.0588	0.0026	0.0052	0.0494	20.3	1.0	1.3	8.7
Site-9-1	0.0179	0.0058	0.0100	0.0509	6.2	2.2	2.6	9.0
Site-9-2	0.0332	0.0045	0.0087	0.0453	11.5	1.7	2.2	8.0
Site-9-3	0.0723	0.0000	0.0021	0.0113	25.0	<LOD	<LOD	2.0
Site-10-1	0.0253	0.0094	0.0152	0.1662	8.8	3.6	3.9	29.3
Site-10-2	0.0544	0.0049	0.0070	0.0546	18.8	1.9	1.8	9.6
Site-10-3	0.0629	0.0026	0.0037	0.0440	21.8	1.0	0.9	7.7
Site-11-1	0.0221	0.0113	0.0212	0.4119	7.7	4.3	5.4	72.5
Site-11-2	0.0269	0.0122	0.0170	0.4592	9.3	4.7	4.4	80.8
Site-11-3	0.0511	0.0032	0.0065	0.1799	17.7	1.2	1.7	31.7
Site-12-1	0.0101	0.0103	0.0171	0.4853	3.5	4.0	4.4	85.4
Site-12-2	0.0478	0.0028	0.0052	0.1961	16.6	1.1	1.3	34.5
Site-12-3	0.0499	0.0031	0.0053	0.1970	17.3	1.2	1.4	34.7
Site-13-1	0.0132	0.0143	0.0183	0.4239	4.6	5.5	4.7	74.6
Site-13-2	0.0175	0.0123	0.0162	0.4259	6.1	4.7	4.1	75.0
Site-13-3	0.0528	0.0040	0.0069	0.1880	18.3	1.5	1.8	33.1
Site-14-1	0.0209	0.0173	0.0269	0.6244	7.2	6.6	6.9	109.9
Site-14-2	0.0745	0.0000	0.0023	0.0966	25.8	<LOD	<LOD	17.0

[a] Raman peak area ratio (PAR) of SO_4^{2-}/H_2O calculated using peak areas of SO band and OH bending band.
[b] Raman peak area ratio (PAR) of CH_4/H_2O calculated using peak areas of CH symmetric stretching band and OH bending band.
[c] Raman peak area ratio (PAR) of H_2S/H_2O calculated using peak areas of HS band and OH bending band.
[d] Raman peak height ratio (PHR) of CO_2/H_2O calculated using peak heights of CO stretching band and OH bending band.
[e] Concentration of dissolved SO_4^{2-} in hydrothermal fluids calculated using Eq. (7) of Li et al., 2018.
[f] Concentration of dissolved CH_4 in hydrothermal fluids calculated using Eq. (1) of Li et al., 2020.
[g] Concentration of dissolved H_2S in hydrothermal fluids calculated using equation of Zhang et al., 2011.
[h] Concentration of dissolved CO_2 in hydrothermal fluids calculated using Eq. (4) of Li et al., 2018.

Table S2. Endmember concentrations of CH_4, H_2S and CO_2 calculated by extrapolating SO_4^{2-} concentration to zero

Endmembers of volatiles	**Site 1**	**Site 2**	**Site 3**	**Site 4**	**Site 5**
CH_4 (mmol/kg)	21.2 ± 1.2	13.0 ± 1.7	16.3 ± 0.8	17.6 ± 0.4	10.1 ± 0.7
H_2S (mmol/kg)	11.1 ± 0.5	6.6 ± 0.6	8.2 ± 0.8	11.8 ± 0.3	10.7 ± 0.7
CO_2 (mmol/kg)	564.8 ± 28.5	299.8 ± 36.1	370.6 ± 2.7	492.4 ± 9.9	196.9 ± 17.4
Endmembers of volatiles	**Site 6**	**Site 7**	**Site 8**	**Site 9**	**Site 10**
CH_4 (mmol/kg)	25.8 ± 1.5	50.9 ± 6.0	6.0± 0.7	3.0 ± 0.3	5.2 ± 0.2
H_2S (mmol/kg)	16.8 ± 1.1	22.7 ± 2.0	5.3 ± 0.1	3.6 ± 0.3	5.5 ± 0.3
CO_2 (mmol/kg)	698.4 ± 25.8	767.1 ± 27.8	36.9 ± 1.2	12.2 ± 0.7	39.7 ± 3.1
Endmembers of volatiles	**Site 11**	**Site 12**	**Site 13**	**Site 14**	
CH_4 (mmol/kg)	6.2 ± 0.6	4.2 ± 0.5	6.2 ± 0.3	8.8 ± 0.1	
H_2S (mmol/kg)	6.8 ± 0.5	4.7 ± 0.4	5.4 ± 0.1	9.2 ± 0.1	
CO_2 (mmol/kg)	106.4 ± 7.3	93.1 ± 2.8	91.1 ± 1.9	147.5 ± 5.1	

Table S3. Results from the flow measurements, volatiles flux and heat output estimates

Vents	Flow velocity (cm/s)	Diffuse/focused flow area (m^2)	Proportion of eruption area	Temperature difference [a] (°C)	Volatile fluxes (mol/year) [b]			Heat flux (MJ/year)
					CO_2	CH_4	H_2S	
Site 1	10.4	67.8	5%-20%	40	3.1-12.6E+10	1.4-5.8E+09	9.3-37.0E+08	5.3-20.9E+10
Site 2	8.2	102.5	5%-20%	33				
Site 3	5.7	84.4	5%-20%	44				
Site 4	13.5	93.1	5%-20%	40				
Site 5	15.5	20.1	5%-20%	86				
Site 6	14.0	24.9	5%-20%	107				
Site 7	12.8	11.4	5%-20%	91				
Site 8	14.0	37.0	5%-20%	260				
Site 9	12.4	71.4	5%-20%	200				
Site 10	24.8	53.7	5%-20%	237				
Site 11	52.4	12.3	1%-5%	256	1.2-5.8E+09	7.0-35.0E+07	7.0-35.1E+07	1.1-5.3E+10
Site 12	29.2	8.7	1%-5%	272				
Site 13	33.3	19.3	1%-5%	296				
Site 14	71.5	19.8	1%-5%	298				

[a] Temperature difference between hydrothermal fluid and ambient seawater.

[b] Estimation error sources: uncertainty of the *in situ* Raman spectroscopy concentration measurements, uncertainty of flow rates and diffuse (focused) flow area estimation, uncertainty in estimating the proportion of the actual eruption area

REFERENCES CITED

Chou, I. M., Pasteris, J. D., and Seitz, J. C., 1990, High-density volatiles in the system COHN for the calibration of a laser Raman microprobe: Geochimica et Cosmochimica Acta, v. 54, p. 535-543, https://doi.org/10.1016/0016-7037(90)90350-T.

Chou, I. M., and Wang, A., 2017, Application of laser Raman micro-analyses to Earth and planetary materials: Journal of Asian Earth Sciences, v. 145, p. 309-333, https://doi.org/10.1016/j.jseaes.2017.06.032.

Dubacq, B., Bickle, M. J., and Evans, K. A., 2013, An activity model for phase equilibria in the H_2O–CO_2–NaCl system: Geochimica et Cosmochimica Acta, v. 110, p. 229-252, https://doi.org/10.1016/j.gca.2013.02.008.

Dubessy, J., Poty, B., and Ramboz, C., 1989, Advances in COHNS fluid geochemistry based on micro-Raman spectrometric analysis of fluid inclusions: European journal of Mineralogy, v. 1, p. 517-534, https://doi.org/10.1127/ejm/1/4/0517.

Dubessy, J., Buschaert, S., Lamb, W., Pironon, J., and Thiéry, R., 2001, Methane-bearing aqueous fluid inclusions: Raman analysis, thermodynamic modelling and application to petroleum basins: Chemical Geology, v. 173, p. 193-205, https://doi.org/10.1016/S0009-2541(00)00275-8.

Li, L., Zhang, X., Luan, Z., Du, Z., Xi, S., Wang, B., Cao, L., Lian, C., and Yan, J., 2018, *In situ* quantitative Raman detection of dissolved carbon dioxide and sulfate in deep-sea high-temperature hydrothermal vent fluids: Geochemistry, Geophysics, Geosystems, v. 19, p. 1809-1823,

https://doi.org/10.1029/2018GC007445.

Li, L., Zhang, X., Luan, Z., Du, Z., Xi, S., Wang, B., Cao, L., Lian, C., and Yan, J., 2020, *In situ* Raman quantitative detection of methane concentrations in deep-sea high-temperature hydrothermal vent fluids: Journal of Raman Spectroscopy, v. 51, p. 2328-2337, https://doi.org/10.1002/jrs.5981.

Lu, W., Chou, I. M., Burruss, R. C., and Song, Y., 2007, A unified equation for calculating methane vapor pressures in the CH_4–H_2O system with measured Raman shifts: Geochimica et Cosmochimica Acta, v. 71, p. 3969-3978, https://doi.org/10.1016/j.gca.2007.06.004.

Lu, W., Chou, I. M., and Burruss, R. C., 2008, Determination of methane concentrations in water in equilibrium with sI methane hydrate in the absence of a vapor phase by *in situ* Raman spectroscopy: Geochimica et Cosmochimica Acta, v. 72, p. 412-422, https://doi.org/10.1016/j.gca.2007.11.006.

Ramondenc, P., Germanovich, L. N., Von Damm, K. L., and Lowell, R. P., 2006, The first measurements of hydrothermal heat output at 9°50′ N, East Pacific Rise: Earth and Planetary Science Letters, v. 245, p. 487-497, https://doi.org/10.1016/j.epsl.2006.03.023.

Rona, P. A., and Trivett, D. A., 1992, Discrete and diffuse heat transfer atashes vent field, Axial Volcano, Juan de Fuca Ridge: Earth and Planetary Science Letters, v. 109, p. 57-71, https://doi.org/10.1016/0012-821X(92)90074-6.

Rosso, K. M., and Bodnar, R. J., 1995, Microthermometric and Raman spectroscopic detection limits of CO_2 in fluid inclusions and the Raman spectroscopic

characterization of CO_2: Geochimica et Cosmochimica Acta, v. 59, p. 3961-3975, https://doi.org/10.1016/0016-7037(95)94441-H.

Seewald, J. S., Doherty, K. W., Hammar, T. R., and Liberatore, S. P., 2002, A new gas-tight isobaric sampler for hydrothermal fluids: Deep Sea Research Part I: Oceanographic Research Papers, v. 49, p. 189-196, https://doi.org/10.1016/S0967-0637(01)00046-2.

Von Damm, K. L., Edmond, J. M., Grant, B., Measures, C. I., Walden, B., and Weiss, R. F., 1985, Chemistry of submarine hydrothermal solutions at 21°N, East Pacific Rise: Geochimica et Cosmochimica Acta, v. 49, p. 2197-2220, https://doi.org/10.1016/0016-7037(85)90222-4.

Wopenka, B., and Pasteris, J. D., 1986, Limitations to quantitative analysis of fluid inclusions in geological samples by laser Raman microprobe spectroscopy: Applied Spectroscopy, v. 40, p. 144-151, https://doi.org/10.1366/0003702864509592.

Zhang, X., Hester, K. C., Ussler, W., Walz, P. M., Peltzer, E. T., and Brewer, P. G., 2011, *In situ* Raman-based measurements of high dissolved methane concentrations in hydrate-rich ocean sediments: Geophysical Research Letters, v. 38, p. L08605, https://doi.org/10.1029/2011GL047141.

Zhang, X., et al., 2017, Development of a new deep-sea hybrid Raman insertion probe and its application to the geochemistry of hydrothermal vent and cold seep fluids: Deep Sea Research Part I: Oceanographic Research Papers, v. 123, p. 1-12, https://doi.org/10.1016/j.dsr.2017.02.005.